Monthly Notices
of the
ROYAL ASTRONOMICAL SOCIETY

MNRAS **435,** 1350–1357 (2013)
Advance Access publication 2013 August 28

doi:10.1093/mnras/stt1377

Shock ionization in the extended emission-line region of 3C 305: the last piece of the (optical) puzzle

V. Reynaldi[1,2]⋆ and C. Feinstein[1,2]⋆

[1]*Facultad de Ciencias Astronómicas y Geofísicas, UNLP, Paseo del Bosque s/n, La Plata 1900, Argentina*
[2]*Instituto de Astrofísica de La Plata, CONICET, Argentina*

Accepted 2013 July 22. Received 2013 July 19; in original form 2013 June 17

ABSTRACT

We present new Gemini spectroscopical data of the extended emission-line region of the 3C 305 radio galaxy in order to achieve a final answer to the long-standing question about the ionizing mechanism. The spectra show strong kinematic disturbances within the most intense line-emitting region. The relative intensities of the emission lines agree with the hypothesis that the gas is shocked during the interaction of powerful radio jets with the ambient medium. The emission from the recombination region acts as a very effective cooling mechanism, which is supported by the presence of a neutral outflow. However, the observed intensity is almost an order of magnitude lower than expected in a pure shock model. So, autoionizing shock models, in low-density and low-abundance regimes, are required in order to account for the observed emission within the region. This scenario also supports the hypothesis that the optical emitting gas and the X-ray plasma are in pressure balance.

Key words: galaxies: active – galaxies: individual: 3C 305 – galaxies: ISM – galaxies: jets.

1 INTRODUCTION

The ionizing mechanism on the optical emission-line regions of powerful radio galaxies is always an interesting topic to debate. Because of their multiwavelength-emitting nature, the radiating power of the active nucleus and the role that jets might play, these objects are fascinating scenarios to test the scope of the two main likely mechanisms: nuclear photoionization and shock ionization. Direct interaction between the radio jets and the optical-emitting gas has been reported in a wide sample of sources from the Third Cambridge Revised Catalogue of Radio Sources (3CR sources; Feinstein et al. 1999; Márquez et al. 2000; Solórzano-Iñarrea, Tadhunter & Bland-Hawthorn 2002; Tilak et al. 2005; Christensen et al. 2006; Hardcastle, Massaro & Harris 2010). However, the traces of such a violent process sometimes remain present within the gas even when those structures seem not to be related (Solórzano-Iñarrea, Tadhunter & Axon 2001; Feinstein et al. 2002; Reynaldi & Feinstein 2013).

The interaction between the radio jets and the interstellar medium (ISM) in 3C 305 has been reported in several multiwavelength investigations, most of which have studied the strongly disturbed kinematics. Optical line-splitting has been used to show the violent processes that the gas within the extended emission-line region (EELR) is undergoing (Heckman et al. 1982; Hardcastle et al. 2012). In an earlier work, Heckman et al. (1982) have already pointed out that the most complex and disordered kinematics of the EELR are located near the most intense radio features, and that the relation between these structures is not restricted to the kinematics. More recently, it has been noticed that the optical gas is not the only ISM phase in 3C 305 that the jet–cloud interaction can alter. H I observations have been fundamental in showing that in such a process (i) the gas clouds are not destroyed by the passing of the relativistic jet, (ii) the high-velocity neutral and ionized clouds are ejected by the same process and (iii) the ambient gas can cool in a very efficient way after being shocked (Morganti et al. 2005). The presence of the [Fe II] λ1.644 μm infrared (IR) emission line, which is spatially coincident with [O III] λ5007, also provides evidence of a shocked medium (Jackson et al. 2003). Towards the other side of the electromagnetic (EM) spectrum, it has been shown that the X-ray emission is strongly related to the [O III] structures in this galaxy, not only by morphological coincidence but also by their possible common origin; that is, the X-ray emission is concentrated below $\sim$2 keV where most of the collisionally excited emission lines are formed (Bianchi, Guainazzi & Chiaberge 2006; Massaro et al. 2009; Hardcastle et al. 2012).

All these self-consistent results reveal that radio (non-thermal), H I-21-cm, IR, optical and X-ray emission not only overlap but are also intrinsically related. The long-standing dichotomy between nuclear photoionization and jet-driven shock-ionization processes within the EELR in 3C 305 is now ending.

In order to finally address this issue, we have obtained new optical spectra of the EELR in 3C 305 with unprecedented spatial and spectral resolution (Section 2). We have chosen to put the slit in roughly the jet direction (the difference is the result of a higher surface brightness over the chosen direction; see Section 3) because we

⋆E-mail: vreynaldi@fcaglp.unlp.edu.ar (VR); cfeinstein@fcaglp.unlp.edu.ar (CF)

Table 1. A set of emission lines in the EELR of 3C 305. Fluxes are relative to that of Hβ for each selected position.

	Flux					
Line (Å)	3.8 arcsec NE	2.6 arcsec NE	1.5 arcsec NE	1.5 arcsec SW	2.6 arcsec SW	3.3 arcsec SW
[O II] λ3727	4.1	4.39	8.34	4.08	3.96	15.66
[Ne III] λ3869	0.79	0.53	0.8	0.63	0.73	–
He II (4686)	–	0.12	–	0.43	–	–
Hβ (4861)	1	1	1	1	1	1
[O III] λ4959	2.08	1.52	2.91	2.74	2.53	6.78
[O III] λ5007	6.2	4.67	8.24	8.44	7.57	20.1
[N I] λ5200	0.19	0.26	0.36	0.51	0.26	–

want to explore the physical conditions of the EELR gas in the same place where the radio jets have been interacting with it. In Section 4, we discuss the main ionizing mechanism, using all the previous results in every EM band as background information. We also add the diagnostic analysis, based on the high-quality emission lines in our new long-slit spectra. In Section 5, we collect all the pieces together to finally solve the puzzle, confirming that jet-induced shocks have triggered the EELR emission.

2 NEW GEMINI/GMOS DATA

We observed 3C 305 ($z = 0.04164$) in 2011 April with the 8-m Gemini North Telescope as part of the GN-2011A-Q-66 programme (PI: Feinstein). The Gemini Multi-Object Spectrograph (GMOS) facility was set up in long-slit mode, placing the 0.75-arcsec-width slit at PA $= 45^\circ$ lying on the optical–ultraviolet emission region. We have used the B600-G5307 grating, $R \sim 1700$, which yields a resolution of 0.9 Å px^{-1}. One exposure of 2400 s was taken with a 2×2 binned CCD. Because the binned spectrum has a resolution of 0.1454 arcsec px^{-1}, it gives a linear scale (using $H_0 = 73$ km s^{-1} Mpc^{-1}, $\Omega_{\rm mat} = 0.27$ and $\Omega_\Lambda = 0.73$) of about 124 pc px^{-1}, without projection correction. The data were reduced following the usual steps of bias subtraction, flat-field correction, wavelength calibration and sky subtraction, using the GEMINI-GMOS package reduction tasks within IRAF.[1] Cosmic ray rejection was not performed because the two available tasks (`gscrrej` from the GEMINI package and the independent `lacos_scpec` task; van Dokkum 2001) sometimes fail to clean the spectrum. We have found some cases where the cosmic ray hit has not been removed and, what is worse, in other cases, the tasks left a hole in the place of the cosmic ray rather than cleaning it. This failure is particulary dangerous when the cosmic ray hits the line profile. For this reason, we have not removed cosmic rays from the entire spectrum. However, they can be eliminated individually over the line profile once the Gaussian decomposition is carried out, and therefore they do not represent an obstacle to the measurements.

The spectral range covers from ∼3600 up to ∼5800 Å. The lines from oxygen ions dominate the spectrum. In Table 1, we list the set of emission lines identified within both the north-east (NE) and south-west (SW) EELR; we also list the fluxes relative to that of Hβ. The angular distances are measured with respect to the galactic centre, which was identified as the peak of intensity within the continuum emission in several featureless regions of the spectrum. The continuum emission drops below the noise in our GMOS spectrum at ∼1 arcsec from the galactic centre, so we have defined the central region as the inner 3 arcsec. In the following analysis, the central region was excluded to prevent our measurement being affected by the stellar component. Many absorption features are also present within this region.

Fig. 1 shows the three most intense lines (i.e. Hβ and the doublet [O III] λλ4959, 5007) in grey-scale, and it reveals how complex the lines are. The contours have been plotted with the aim of emphasizing the line's intrinsic shapes. The dot-like feature superimposed on the [O III] λ5007 line at around 5010 Å is not part of the line's structure but is a cosmic ray hit. The [O III] λ5007 emission extends up to 15 arcsec towards the NE and 9 arcsec to the SW, although this is not shown in the figure because of its low intensity. These tails are only detected in [O III] λ5007.

3 RESULTS

We can find almost all the emission concentrated inside ±4 arcsec (∼6.8 kpc) from the nucleus, but the tails of the [O III] λ5007 emission reveal that the optical-emitting gas is extended as much as the X-ray emission (Hardcastle et al. 2012). The total extension of the line emission along the slit direction (PA $= 45^\circ$, north to east) is then 24 arcsec (∼20 kpc). The radio axis location lies in roughly the same direction (PA $= 42^\circ$; Morganti et al. 2005). The peaks of line emission are offset from the nuclear region, as found by Heckman et al. (1982); there is a maximum of emission towards the NE at 2–3 arcsec, and a second weaker maximum at the same distance towards the SW. The NE knot in our spectrum lies near the NE radio hotspot, and there is also a bright X-ray feature at the same place (see figs 3 and 4 of Hardcastle et al. 2012).

The complexity in the kinematics of the region has already been pointed out, not only in the ionized gas but also in H I (Morganti et al. 2005). So, as expected, the line profiles are also kinematically complex in our Gemini spectrum. We have extracted the one-dimensional spectra in a pixel-by-pixel way to avoid the loss of spatial information. We have fully discussed the Gaussian decomposition in an earlier paper (Reynaldi & Feinstein 2013). Up to three Gaussian components were needed in order to fit the [O III] λ5007 profile in the NE region. The structure of the SW region appears to be simpler than that of the NE region in the long-slit spectrum (Fig. 1); actually, the NE region displays not only the strongest emission but also the most disturbed motion. However, the Gaussian decomposition in the SW EELR has also revealed more than one component. Fig. 2 shows our velocity field, which was computed from the [O III] λ5007 decomposition. The velocities are expressed with respect to the host galaxy systemic velocity. Because the central region was excluded (Section 2), there are no data inside the inner 3 arcsec; the cross indicates the galactic centre. The most kinematical complexity, and therefore the most disturbed motion, appears towards the NE, in agreement with the Hα velocity field from Morganti et al. (2005). Despite the difference of 3° in the

[1] IRAF is distributed by the National Optical Astronomy Observatories, which are operated by the Association of Universities for Research in Astronomy, Inc., under cooperative agreement with the National Science Foundation.

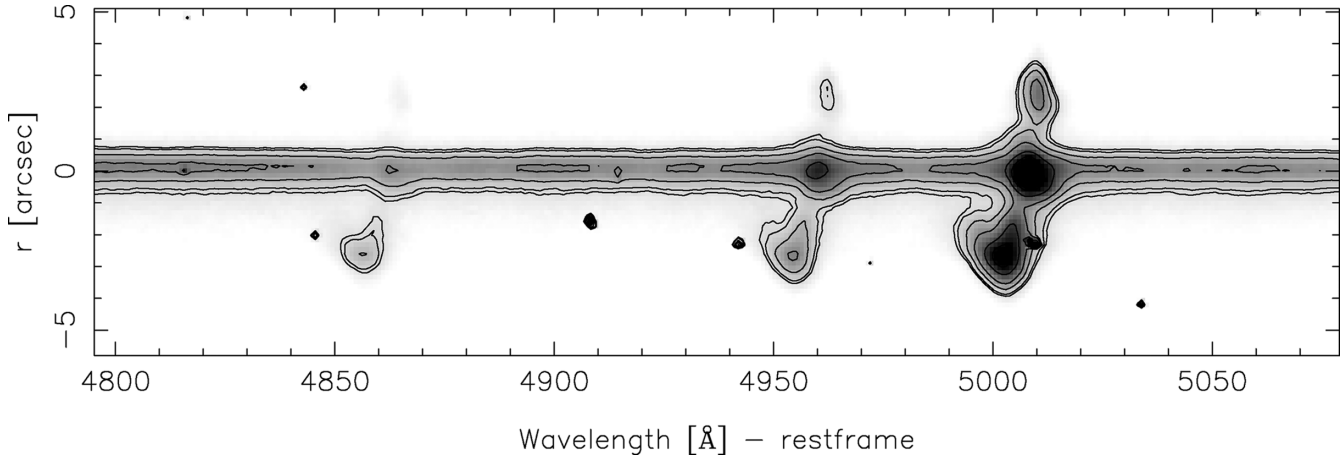

Figure 1. A section of the long-slit Gemini spectrum. The lines are Hβ and the doublet [O III] $\lambda\lambda$4959, 5007. The ordinate scale indicates the NE (negative) and SW (positive). The contour levels are shown only to emphasize the grey-scale contrast. There are tails of [O III] λ5007 low-brightness emission extending up to 15 arcsec NE and 9 arcsec SW, which are not shown here.

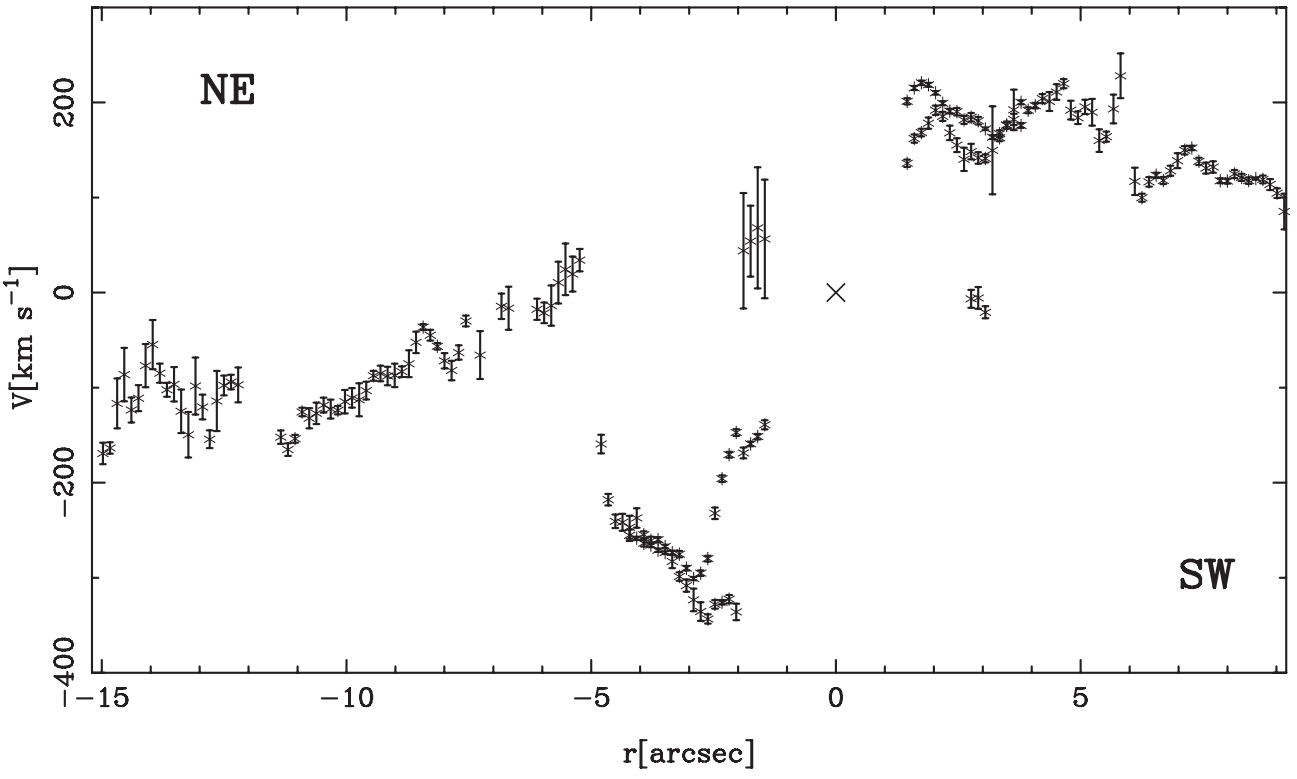

Figure 2. Velocity field computed from the components that form the [O III] λ5007 emission-line profile. The cross indicates the galactic centre.

position angles with which our spectra and theirs were taken, we note that the high-velocity [O III] components are located between 2 and 5 arcsec, slightly further away from the nucleus than the Hα high-velocity components. While the rotation curve becomes stable at around $\sim\pm200\,\mathrm{km\,s^{-1}}$, the blueshifted line-splitting in the NE region accounts for strongly disturbed movements that reach radial velocities of $\sim400\,\mathrm{km\,s^{-1}}$.

In multiwavelength studies of 3C 305, including the overlapping of its emission (or absorption, in the case of H I) and the overall kinematics, it has been pointed out that the radio jet is interacting with the ambient medium in a violent way. In the optical band, the main clues about such an interaction have come from a kinematical point of view. In the following section, we aim to show that the kinetical energy transferred by the jets into the ISM also drives shock waves that ionize the gas.

4 IONIZING MECHANISM

We investigate whether the jet–cloud interaction can leave its trace in the ionization state of the region. The first spectral signature of shocks came from the [Fe II] λ1.644 μm IR emission line reported by Jackson et al. (2003). This line, first discovered in supernova remnants, is produced by collisional excitation with electrons. The strong shock waves triggered by the supernova explosion give rise to synchrotron emission within the recombination region. The iron

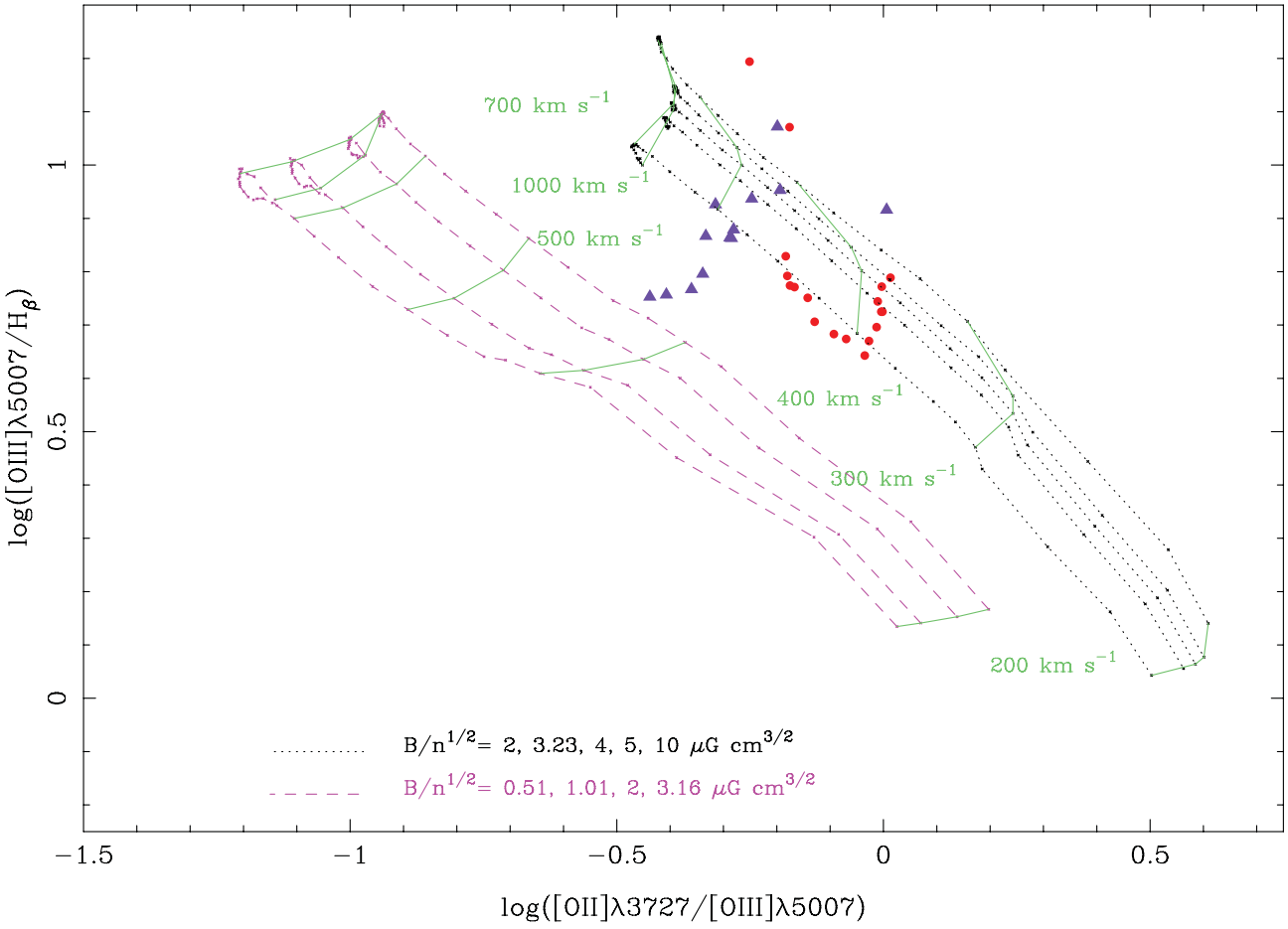

Figure 3. Grids of the shock-ionization (solar abundance) model (Allen et al. 2008) for two different ambient densities: 100 cm^{-3} as dotted lines and 1000 cm^{-3} as dashed lines. There is one line per magnetic parameter. The same values were used in both plots, but note that they differ depending upon density; the magnetic field strength was restricted to $16 < B < 100$ μG (see text). The NE EELR is plotted as dots (red dots in the electronic version) and the SW EELR is plotted as triangles (violet triangles in the electronic version).

line is excited by this same electron population, and thus near-IR and radio emission are overlapped in this case (Kawara, Taniguchi & Nishida 1988; Moorwood & Oliva 1988; Greenhouse et al. 1991; Forbes & Ward 1993). The spatial relation between radio and [Fe II] emission in 3C 305 was shown by Jackson et al. (2003), who argued that the presence of shocks is evident at the jet termination point, where [Fe II] emission reaches its maximum. In addition, they have also shown that [Fe II] and [O III] λ5007 emission are overlapped and extended along the radio axis, although the oxygen emission is more extended. Because our Gemini spectrum was specially obtained in a direction roughly coincident with that of the radio axis, we can investigate whether the jets were able to trigger not only the [Fe II] emission but also the entire EELR emission through autoionizing shocks.

The passing of the radio jets drives shock waves within the medium where it propagates. As a result, the gas is heated and accelerated. The heating gives rise to emission, as a cooling mechanism. Also, because the clouds are accelerated, additional (secondary) shock waves might be created by the strong cloud–cloud interaction that occurs within the clumpy medium (Heckman et al. 1982). Although strongly dependent on velocities, the jets can also trigger autoionizing shocks. In such a case, these shocks will collisionally ionize the gas, as well as photoionizing the gas ahead of the shock. The contribution of this pre-ionized gas to the whole spectrum will depend on how fast the shock moves (Dopita & Sutherland 1995, 1996; Allen et al. 2008). Now, we want to analyse the influence of a local radiation field created *in situ* by this type of shock wave driven by the radio jet.

The shock-ionization models (solar abundances) from Allen et al. (2008) were used in the diagnostic diagrams plotted in Figs 3–5. We have plotted the shock+precursor grids (i.e. autoionizing shocks) for two values of pre-shock density n: 10^2 cm^{-3} (dotted lines) and 10^3 cm^{-3} (dashed lines). The ambient density has been constrained by using optical lines, but it has been calculated under photoionization conditions (case B; Osterbrock 1989). Morganti et al. (2005) derived $n < 500$ cm^{-3} by using [S II] λλ6717,6731, but Heckman et al. (1982) had previously found 1000 cm^{-3} with the same line ratio, although some uncertainties might have affected the result. Because this is the only information we have regarding the optical band, we use the shock-ionization grids with 10^2 and 10^3 cm^{-3} as extreme density values. However, it is worth noting that the density might be very different under shock-ionization conditions. The shock-only (non-autoionizing) grids lie outside the region covered by our observations, so these were not plotted. Each curve is characterized by one magnetic parameter, the $B/n^{1/2}$ value, where B is the magnetic field strength. Hardcastle et al. (2012) have constrained the magnetic field strength from radio depolarization and X-ray measurements, giving $16 < B < 100$ μG. We have traced the

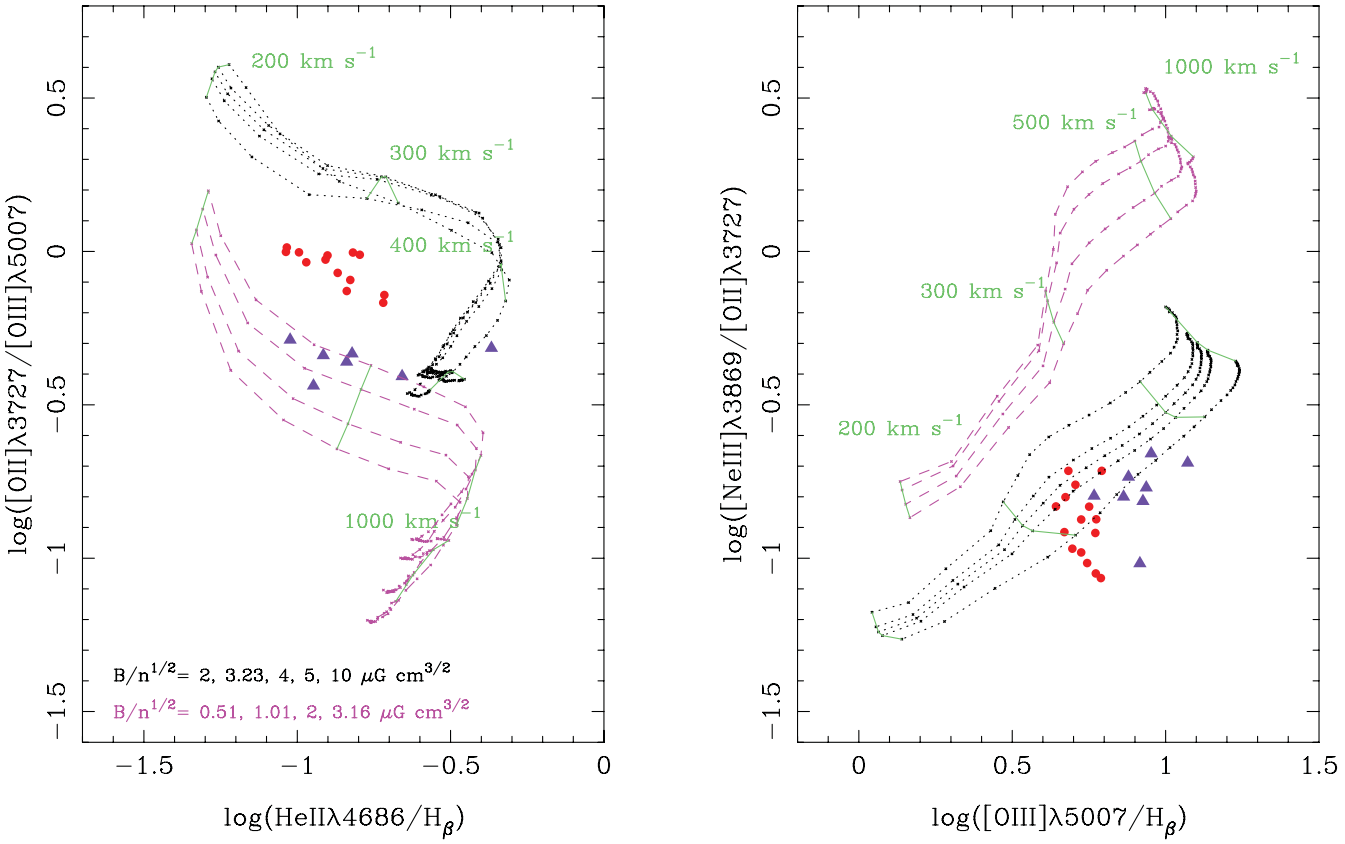

Figure 4. Grids of solar abundance shock-ionization models. The [O II] λ3727/[O III] λ5007 and [Ne III] λ3869/Hβ ratios are very sensitive to the pre-shock density when combined with [O III] λ5007/Hβ and He II/Hβ. See also Fig. 3 for model and data references.

curves whose magnetic field lies in this range. The shock velocities are also pointed out (straight lines).

Each EELR was plotted separately, the NE region as dots and the SW region as triangles. The diagrams combine high- and low-excitation lines, with He II and [Ne III] λ3869 being the highest excitation lines in the spectrum. The observations are well fitted by the models, regardless of the way in which the line ratios are formed. The NE and SW data sets are clearly detached from each other, mostly because of their [O II] λ3727/[O III] λ5007 intensity.

The models reproduce the observed relative intensities if the shock propagates at $300 < v < 500\,\mathrm{km\,s^{-1}}$ (i.e. the same disturbed velocities that we find in the velocity field). Lines such as [O II] λ3727 and Hβ are particularly intense. These low-ionization lines are usually formed within the recombination region behind the shock front. This is the place where the bulk of collisional excitation lines are formed. However, if we consider just the emission coming from the recombination region, then we should find significantly lower intensities, almost an order of magnitude lower than those observed in the [O II] λ3727/[O III] λ5007 and [O III] λ5007/Hβ ratios. It is also worth highlighting the fact that, although different mean values characterize each EELR, the [O II] λ3727/[O III] λ5007 line ratio remains almost constant within each region (see Fig. 3 and the left panel of Fig. 4). This is an important result because it implies that the ionizing conditions are not changing within the inner ±4.5 arcsec (±4 kpc) approximately.

Regarding the [O II] λ3727/[O III] λ5007 and [Ne III] λ3869/[O II] λ3727 line ratios (Figs 3 and 4), both the theoretical behaviour and the observed behaviour deserve special attention and we discuss these in Sections 4.1 and 4.2.

4.1 Why the EELR is not photoionized?

We wonder if we can explain such an enhancement in the [O II] λ3727 emission as an improvement on the nuclear ionizing power once the shocks have passed throughout the EELR clouds. Nuclear photoionization might certainly play a role, but it has to be of secondary relevance in the case of 3C 305, because it is hard to reconcile with these three important clues.

(i) The ionization state of the region does not drop with radial distance, as stated by Heckman et al. (1982) and confirmed with our new data. The intensity profiles peak at 2–3 arcsec (∼2 kpc) from the nucleus, including the high-excitation He II, [Ne III] λ3869, or [O III] λ5007 lines. However, the most important clue in this regard is the way in which [O II] λ3727/[O III] λ5007 behaves. As we have already said, it remains quite constant, showing no evidence of spatial variation. If the ISM were photoionized, the geometrical dilution of photons should be mirrored by this line ratio (see Penston et al. 1990, and references therein). This means that spectral variation as a function of distance from the nucleus should be noticeable. In the same sense, the X-ray hardness ratio (Hardcastle et al. 2012) does not show spatial variation, which implies that no spectral variation can be inferred from this EM band either. In other words, the lack of ionizing photons with increasing distance, which is characteristic of photoionization, is not observed in the optical or X-rays.

(ii) The kinematics show that most disturbed components are found at almost the same location as the maximum line intensity.

(iii) The X-ray extended emission was successfully reproduced by collisional ionization. It is worth emphasizing at this point that

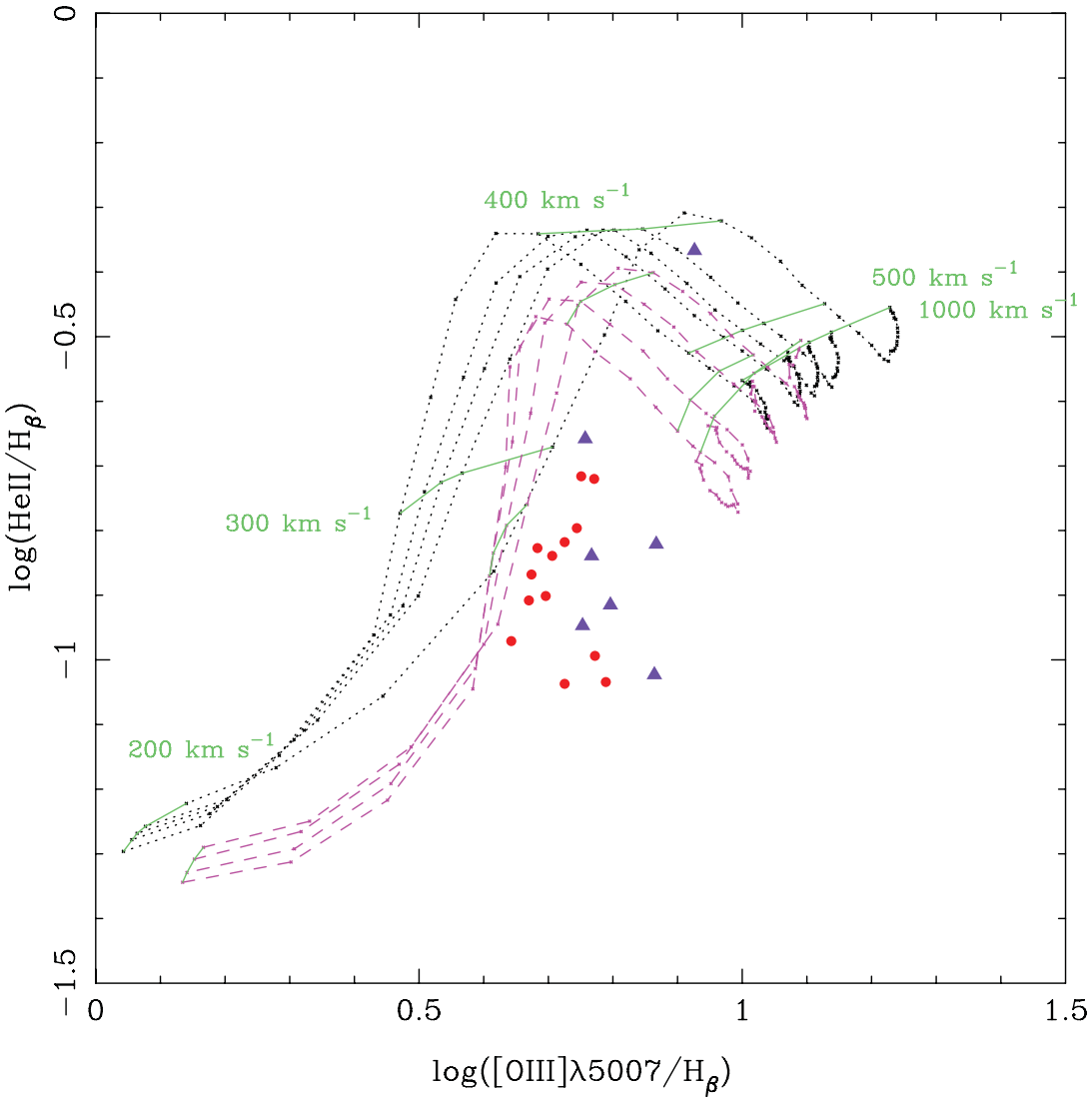

Figure 5. Density information is lost when [O III] λ5007/Hβ and He II/Hβ ratios are combined in the same diagram. Models and data as in Fig. 3.

both optical and soft X-ray emission might have the same origin (Bianchi et al. 2006; Massaro et al. 2009; Hardcastle et al. 2012).

4.2 Ambient density

The theoretical grids clearly show that the oxygen ratio and [Ne III] λ3869/[O II] λ3727, when combined with [O III] λ5007/Hβ and He II/Hβ, are strongly sensitive to the pre-shock density (Figs 3 and 4). None of these latter ratios provides any information about density when combined with another (Fig. 5), but the ratios are useful in separating the grids. On the whole, the observations are best reproduced by low-density models.

An interesting result is found when [O II] λ3727/[O III] λ5007 and [Ne III] λ3869/[O II] λ3727 are combined in the same diagram. The grids overlap each other, so the diagram is completely degenerated in density.[2] Such a degeneracy can be broken up, for instance, with He II/Hβ or [O III] λ5007/Hβ in a three-dimensional diagram. Because the huge MAPPING III data base (Allen et al. 2008) is comprised of several data sets of densities and abundances, we have been able to test different types of scenario. Other combinations of density and metallicity, besides those used in the previous diagrams, were studied. In the next paragraph, we explain these changes, and the reason why they were tested for. The key point here is that if He II/Hβ is used instead of [O III] λ5007/Hβ, the degeneracy is simultaneously solved for density and abundance too, if shock velocities are slower than 700 km s^{-1}.

Hardcastle et al. (2012) have suggested that the X-ray plasma and the line-emitting gas might be in rough pressure balance. Under this hypothesis, the temperature in the ionized gas ($T \gtrsim 10^4$ K) limits the density to the range $n \lesssim 180$ cm^{-3} (this is a crude estimation because we did not take into consideration the X-ray or line-emitting volumes). Nevertheless, we should emphasize that the X-ray temperature and density (from which the optical temperature and density relation is derived) were obtained for a subsolar abundance gas. For this reason, we have examined the autoionizing shock-model data base in order to adapt the models to the physical conditions derived from the pressure-balance hypothesis.

[2] We do not show this diagram because it would be illegible. However, it can easily be built with the ITERA code from Groves & Allen (2010).

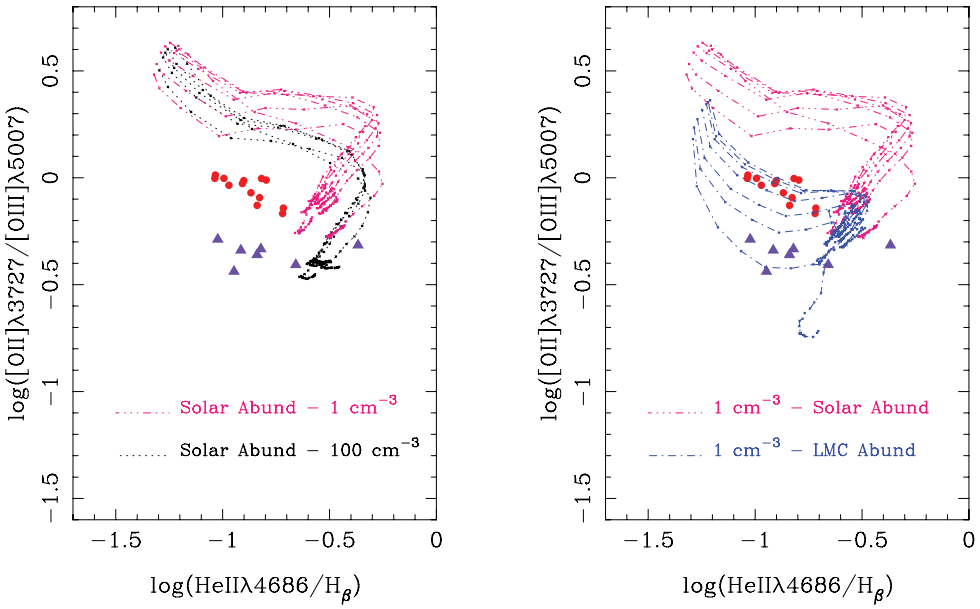

Figure 6. Comparison of densities and abundances in shock-ionization models: dotted lines, solar abundance, 100 cm^{-3} (the same as the previous diagrams); dot-dot-dashed lines, solar abundance, 1 cm^{-3}; dot-dashed lines, LMC abundance (see Allen et al. 2008), 1 cm^{-3}. Left panel: the abundance is fixed to the solar value, while the density varies. Right panel: the density is fixed to 1 cm^{-3}, while the abundance decreases. As in the previous figures, the NE EELR is plotted as dots (red dots in the electronic version) and the SW EELR is plotted as triangles (violet triangles in the electronic version). The data are best reproduced by low-density and low-abundance models, which support the hypothesis that X-ray plasma is in pressure balance with the optical plasma (see text).

The projection on to the [O II] λ3727/[O III] λ5007–He II/Hβ plane (Fig. 6) is the most clear way of viewing the three-dimensional diagram that we mentioned previously ([O II] λ3727/[O III] λ5007 versus [Ne III] λ3869/[O II] λ3727 versus He II/Hβ). For simplicity, we have only drawn the way in which the density behaves when the abundance is fixed to the solar value (left panel) and the way in which the abundance behaves when the density is fixed to $n = 1\,cm^{-3}$ (right panel). The density range tends to favour low densities, so we have chosen $n = 1\,cm^{-3}$ because it is the lowest density value in the library that allowed us to perform the comparison. The following parameter combinations were tested:

(i) solar abundance, $n = 100\,cm^{-3}$ (dotted lines, as in previous diagrams);
(ii) solar abundance, $n = 1\,cm^{-3}$ (dot-dot-dashed lines);
(iii) Large Magellanic Cloud (LMC; see Allen et al. 2008) abundance, $n = 1\,cm^{-3}$ (dot-dashed lines).

The LMC abundance plays the role of the subsolar abundance found by Hardcastle et al. (2012). In order to simplify the diagram, we have not plotted the shock velocities or the magnetic parameters. We have used the same ranges as in the previous figures. The left panel of Fig. 6 shows that it is not enough to lower the density if we want to reproduce the line ratios when we keep the solar abundance. The observations are successfully reproduced when both the density and the abundance are lowered (Fig. 6, right panel), strongly supporting the pressure-balance hypothesis. In addition, an ambient density of around 1 cm^{-3} implies that the temperature should be $T \sim 10^6$ K in the ionized gas. Indeed, this is the characteristic temperature of the high-temperature radiative zone and the non-equilibrium cooling zone of the shock (for a detailed description, see Dopita & Sutherland 1996; Allen et al. 2008), where the models predict the ultraviolet and soft X-ray emission.

5 SUMMARY AND CONCLUSIONS

We have made a detailed analysis of the physical conditions of the EELR in 3C 305. In a large set of previous and self-consistent multiwavelength studies, it has been shown that the gas has been disturbed and also shock-heated by the interaction with the radio jet. We have analysed the ionization condition of the EELR's material following two steps. First, we have discussed the shock-ionization models under density constraints obtained within the line-emitting gas. We have found that the observations are better reproduced by low-density grids in the range $300 < v < 500\,km\,s^{-1}$. The low-ionization lines in the spectrum are especially intense, which implies that the recombination region behind the shock front contributes significantly to the whole emission. However, in order to explain the observed intensities, the contribution from the precursor region is crucial. Secondly, based upon the X-ray parameters determined by Hardcastle et al. (2012), and following the hypothesis that the X-ray plasma is in pressure balance with the EELR's gas, we have explored how the models respond to changes in density and abundance. We have found that the best fit to the observations is reached when shock waves propagate throughout a low-density and low-metallicity medium. The metallicity in our models (LMC) is comparable to that derived from the X-ray study (0.1–0.2 solar). The pressure-balance hypothesis establishes a relationship between density and temperature in the optical band, where our best-fitting density (1 cm^{-3}) implies a high temperature ($\sim 10^6$ K). However, such a temperature is characteristic of the recombination region just behind the shock front, where the bulk of low-ionization lines are formed.

The enhancement in line emission, shown by our new Gemini data, is directly explained by the interaction between the powerful jets and the ambient medium through strong shocks. The high amount of mechanical energy injected in the system drives very fast shock waves. The fastest shocks create a local radiation field whose

power is directly related to the shock velocity: the faster the shock, the harder the ionizing spectrum (see fig. 1 of Allen et al. 2008). The photons created *in situ* ionize the ambient medium before it is reached by the shock (the precursor). The precursor is capable of producing a large amount of emission, in addition to that produced within the recombination region. In this sense, the effectiveness of cooling has to be highlighted by the presence of neutral outflow (Morganti et al. 2005).

The traces of the radio jets throughout the ISM are now being unveiled. The input of mechanical energy not only accelerates the EELR's clouds, but also plays a very important role in triggering the optical line emission and presumably the soft X-ray emission too. With this analysis, we intend to achieve the final step in understanding how the radio components relate to the optical emitting gas; we have found the missing optical piece in the whole picture that Hardcastle et al. (2012) have described. The shock waves driven by the interaction between the radio jet and the ambient gas have had consequences in every EM band.

ACKNOWLEDGEMENTS

This work is based on observations obtained at the Gemini Observatory, which is operated by the Association of Universities for Research in Astronomy, Inc., under a cooperative agreement with the National Science Foundation (NSF) on behalf of the Gemini partnership: the NSF (United States), the Science and Technology Facilities Council (United Kingdom), the National Research Council (Canada), CONICYT (Chile), the Australian Research Council (Australia), Ministério da Ciência, Tecnologia e Inovação (Brazil) and Ministerio de Ciencia, Tecnología e Innovación Productiva (Argentina).

REFERENCES

Allen M. G., Groves B. A., Dopita M. A., Sutherland R. S., Kewley L. J., 2008, ApJS, 178, 20
Bianchi S., Guainazzi M., Chiaberge M., 2006, A&A, 448, 499
Christensen L., Jahnke K., Wisotzki L., Sánchez S. F., Exter K., Roth M. M., 2006, A&A, 452, 869
Dopita M. A., Sutherland R. S., 1995, ApJ, 455, 468
Dopita M. A., Sutherland R. S., 1996, ApJS, 102, 161
Feinstein C., Macchetto F. D., Martel A. R., Sparks W. B., McCarthy P. J., 1999, ApJ, 526, 623
Feinstein C., Macchetto F. D., Martel A. R., Sparks W. B., 2002, ApJ, 565, 125
Forbes D. A., Ward M. J., 1993, ApJ, 416, 150
Greenhouse M. A., Woodward C. E., Thronson H. A., Jr, Rudy R. J., Rossano G. S., Erwin P., Puetter R. C., 1991, ApJ, 383, 164
Groves B. A., Allen M. G., 2010, New Astron., 15, 614
Hardcastle M. J., Massaro F., Harris D. E., 2010, MNRAS, 401, 2697
Hardcastle M. J. et al., 2012, MNRAS, 424, 1774
Heckman T. M., Miley G. K., Balick B., van Breugel W. J. M., Butcher H. R., 1982, ApJ, 262, 529
Jackson N., Beswick R., Pedlar A., Cole G. H., Sparks W. B., Leahy J. P., Axon D. J., Holloway A. J., 2003, MNRAS, 338, 643
Kawara K., Taniguchi Y., Nishida M., 1988, ApJ, 328, L41
Márquez I., Pécontal E., Durret F., Petitjean P., 2000, A&A, 361, 5
Massaro F. et al., 2009, ApJ, 692, L123
Moorwood A. F. M., Oliva E., 1988, A&A, 203, 278
Morganti R., Oosterloo T. A., Tadhunter C. N., van Moorsel G., Emonts B., 2005, A&A, 439, 521
Osterbrock D. E., 1989, Astrophysics of Gaseous Nebulae and Active Galactic Nuclei. University Science Books, Mill Valley, CA
Penston M. V. et al., 1990, A&A, 236, 53
Reynaldi V., Feinstein C., 2013, MNRAS, 430, 2221
Solórzano-Iñarrea C., Tadhunter C. N., Axon D. J., 2001, MNRAS, 323, 965
Solórzano-Iñarrea C., Tadhunter C. N., Bland-Hawthorn J., 2002, MNRAS, 331, 673
Tilak A., O'Dea C. P., Tadhunter C., Wills K., Morganti R., Baum S. A., Koekemoer A. M., Dallacasa D., 2005, AJ, 130, 2513
van Dokkum P. G., 2001, PASP, 113, 1420

This paper has been typeset from a TEX/LATEX file prepared by the author.